

TOP-DOWN CONSTRAINING THE ESTIMATES OF ANTHROPOGENIC AEROSOL
EMISSIONS AND THE PARAMETERIZATION OF DUST SOURCES

by

Xiaoguang Xu

A DISSERTATION

Presented to the Faculty of
The Graduate College at the University of Nebraska

In Partial Fulfilment of Requirements

For the Degree of Doctor of Philosophy

Major: Earth & Atmospheric Sciences
(Meteorology/Climatology)

Under the Supervision of Professor Jun Wang

Lincoln, Nebraska

May, 2015

Table of Contents

List of Figures	v
List of Tables	viii
1 Introduction	1
1.1 Background and Motivation	1
1.1.1 Top-down versus bottom-up	2
1.1.2 Satellite Observations of Aerosol	5
1.2 Main Goals of This Work	5
1.3 Organization of This Dissertation	7
2 Top-Down Inversion Framework	8
2.1 Inversion Theory and Infrastructure	8
2.2 GEOS-Chem Forward Modeling	11
2.2.1 Anthropogenic aerosol emissions	11
2.2.2 Dust emissions	11
2.3 GEOS-Chem Adjoint Modeling	12
3 Optimizing Species-Specified Aerosol Emissions	14
3.1 Introduction	14

3.2	Constraints from Satellite Radiances	16
3.3	Selection of Emissions for Optimization and Sensitivity Tests	16
3.4	Inversion Results	16
3.5	Results Evaluations	16
3.6	Implications of Results	16
3.7	Summary	16
4	Optimizing Dust Source Parameterization	26
4.1	Introduction	26
4.2	Necessary Implementations	27
4.2.1	Development of the wind speed distribution	27
4.2.2	AOD observation operator	30
4.2.3	Adjoint for Dust Flux Parameterization	30
4.3	Constraints from Multi-Satellite Observations	31
4.4	Experiment Design	31
4.5	Constrained Dust Emission Scheme	31
4.6	Validations	31
4.7	Summary	31
5	Summary and Outlook	32
5.1	Summary of the Dissertation	32
5.2	Main Conclusions of This Work	32
5.3	Outlook and Future Work	32
A	Abbreviations and Acronyms	33
B	Symbols	34

References**35****List of Publications****39**

List of Figures

3.1	Flowchart of the proposed top-down inversion framework.	15
3.2	Relative changes in posterior aerosol emissions from <i>a priori</i> in the pseudo-observation experiment. Six panels are respectively for anthropogenic emissions of SO ₂ , NH ₃ , NO _x , BC, and OC, and mineral dust from both natural and anthropogenic sources. The red box in panel (a) indicates the region where AOD observations are selected.	17
3.3	Comparison of the prior (a) and posterior (b) GEOS-Chem (GC) simulation of 0.65 μ m AOD with the AOD at the same wavelength retrieved from MODIS reflectance using GEOS-Chem aerosol optical properties (c) averaged for the period of April 2008. Satellite retrievals with 10 km by 10 km at nadir are aggregated to GEOS-Chem grid cells; and the model AOD are sampled coincidentally with those retrievals. Panel (d) and (e) respectively show the difference of prior and posterior simulated from the satellite retrieved AODs. The red box in panel (c) indicates the region where AOD observations are selected.	17
3.4	(a) Time series of the spatially averaged daily MODIS AOD retrievals (purple) for April 2008 over the Eastern China, compared by the prior (orange) and posterior (green) spatial averaged daily GEOS-Chem AOD that are sampled in the MODIS AOD tempo-spatial space. (b) Time series of the expected daily AOD adjustments (orange) that are the differences between MODIS AOD and the prior GEOS-Chem AOD and their real adjustments (green) that are the differences of posterior from prior GEOS-Chem AOD. (c) Time series of the prior (orange) and posterior (green) daily dust emissions over China for April 2008.	18

3.5	The prior (or bottom-up based, left column), optimized (or top-down constrained, middle column) aerosol emissions over China for the period of April 2008, and their relative differences (right column). Six rows from top to bottom are respectively for anthropogenic emissions of SO_2 , NH_3 , ceNO_x , BC, and OC, and mineral dust from both natural and anthropogenic sources.	19
3.6	(a – i) Scatterplots of GEOS-Chem AOD versus AERONET AOD at $0.55 \mu\text{m}$ prior (red scatters) and posterior (green scatters) to the aerosol emission optimization over nine stations. AERONET AODs are 3-hour averages following the GEOS-Chem output frequency. (j) The overall comparison for eight AERONET sites excluding Beijing. Also shown are the number of valid sampled pairs (n), correlation coefficients (R), bias, and root-mean-square-error (rmse).	20
3.7	Comparison of the prior and posterior GEOS-Chem simulation of $0.55 \mu\text{m}$ AOD with the level 3 MISR $0.55 \mu\text{m}$ AOD for the period April 2008. (a) The prior GEOS-Chem $0.55 \mu\text{m}$ AOD that are sampled coincidentally with MISR AODs for the period of April 2008. Also overlaid circles are the monthly AOD averages at $0.55 \mu\text{m}$ observed from the nine AERONET sites shown in Figure 3.6. (b) Same as (a) but for the monthly average of posterior GEOS-Chem AOD. (c) Monthly average of the Level 3 daily MISR $0.55 \mu\text{m}$ AOD. (d) Scatter plot the GEOS-Chem AOD versus the MISR AOD before (red scatters) and after optimization (green scatters), in which each point indicates an AOD pair over a model grid cell with value over 0.2. Also shown are the statistics including number of sampled pairs (n), correlation coefficient (R), bias and root-mean-square-error (rmse). Comparisons of the monthly GEOS-Chem AOD versus AERONET AOD are also included as the black circles; each circle indicates an AOD pair over an individual site.	21
3.8	Same as figure 3.7 but for comparison of the GEOS-Chem SO_2 simulation with OMI column SO_2 retrievals for the period of April 2008. The OMI planetary boundary layer (PBL) column SO_2 from the Level 3 daily products with 0.25° by 0.25° resolutions are aggregated into GEOS-Chem grid cells.	22
3.9	Same figure 3.7 but for comparison of the GEOS-Chem NO_2 simulation with OMI column NO_2 retrievals for the period of April 2008. The OMI tropospheric column NO_2 from Level 2 daily products with 0.25° by 0.25° resolutions are aggregated into GEOS-Chem grid cells.	23

3.10	Comparison of the GEOS-Chem surface mass concentration of sulfate-nitrate-ammonium (SNA) aerosols with ground-based observations over Qingdao (120.34° E, 36.06° N), China. Discontinuity in time series is due to missing or quality filtered observations.	23
3.11	Time serial plot of the GEOS-Chem simulated surface PM ₁₀ concentrations by prior (red) and posterior (red) aerosol emissions compared with the <i>in situ</i> measured PM ₁₀ (black) over Zhangye (a) and SACOL (b) stations for 15 – 30 April 2008; also shown are the average values over same the period. Discontinuity in time series is due to missing or quality filtered observations.	24
3.12	Taylor diagram for the model evaluations before (squares) and after (circles) optimization when comparing against (1) AERONET AOD at 0.55 μ m, (2) MISR 0.55 μ m AOD, (3) OMI column SO ₂ , (4) OMI column NO ₂ , (5) surface SNA concentrations at Qingdao site, and (6) surface PM ₁₀ concentrations measured at Zhangye and SACOL sites. The color coded on each point indicates the relative bias. It should be noted that the ratio of standard deviations and correlation coefficient between prior GEOS-Chem simulated and measured surface PM ₁₀ over Zhangye and SACOL are 6.5 and 0.45, which makes the point number 6 for the prior simulation far beyond the range of this Taylor diagram.	25
3.13	Change of April monthly 0.55 μ m AOD from 2006 to 2008 from MODIS (a) and MISR (b) Level 3 daily products.	25

List of Tables

1.1	List of satellite sensors with measurement specifications relevant for operation retrieval of aerosol properties.	5
-----	--	---

CHAPTER 1

INTRODUCTION

1.1 Background and Motivation

Atmospheric aerosols play a crucial role in the global climate change. They affect earth energy budget directly by scattering and absorbing solar and terrestrial radiation, and indirectly through altering the cloud formation, lifetime, and radiative properties [Haywood and Boucher, 2000; Ramanathan et al., 2001]. However, quantification of these effects in the current climate models is fraught with uncertainties. The global average of aerosol effective radiative forcing (ERF) were estimated to range from -0.1 to -1.9 Wm² with the best estimate of -0.9 Wm² [Boucher et al., 2013], indicating that the cooling effects of aerosol might counteract the warming effects of 1.820.19 Wm² caused by the increase of carbon dioxide since the industrial revolution [Myhre et al., 2013]. The climate effects of aerosol particles depend on their geographical distribution, optical properties, and efficiency as cloud condensation nuclei (CCN). Key quantities pertain to the aerosol optical and cloud-forming properties include particle size distribution (PSD), chemical composition, mixing state, and morphology [Boucher et al., 2013]. While the daily aerosol optical depth (AOD) can be well measured from current satellite and ground-based remote sensing instrumentations [e.g., Holben et al., 1998; Kaufman et al., 2002], the accurate quantification of aerosol ERF is in no small part hindered by our limited knowledge about the aerosol PSD and refractive index (describing chemical composition and mixing state). To fully understand the role of

aerosol particles in the global climate change, further development in observations along with retrieval algorithms for these aerosol microphysical properties from different platforms are thus highly needed [Mishchenko et al., 2004], and the focus of this two-part series study is the characterization of aerosol properties from ground-based passive remote sensing [Henze et al., 2007].

Dust acts as medium in iron cycle on the earth [Jickells et al., 2005].

The long-distance transport of bacteria together with dust has been discussed in several studies as a mechanism for the global dispersion of microbial species, with the potential to impact ecosystems and public health [Griffin et al., 2001; Burrows et al., 2009]

In the following paragraphs of this section, I briefly describe the impacts of dust aerosols on the earth system, the basic physics of dust emissions, and the current state of satellite remote sensing of mineral dust. Subsequently, I present the specific scientific objectives and the organization of this thesis.

1.1.1 Top-down versus bottom-up

Current estimates of aerosol emissions are largely based on the “bottom-up” method that integrates diverse information such as fuel consumption in various industries and corresponding measurements of emission rates for different species [Streets et al., 2003], economic growth, and the statistics of land use and fire-burned areas [van der Werf et al., 2006]. While significant progress has been made [Streets et al., 2006], the “bottom-up” approach has a number of limitations. First, the emission inventory usually has a temporal lag of at least 2 to 3 years, as time is needed to aggregate information from different sources and format them into the emission inventories that are suitable for use in climate models. Second, the temporal resolution of the current emission inventory is usually on monthly to annual scale, which is not sufficient to characterize the daily or diurnal variation of emissions;

the aerosol impact on radiative transfer and the variation of cloud properties, however, is often strongly dependent on the time of the day [Wang et al., 2006]. Third, the spatial resolutions of the bottom-up emission inventories are usually limited by the availability of the ground-based observations, which often lack the spatial coverage for estimating emission in a uniformly fine resolution for regional modeling of aerosol transport. Finally, bottom-up emission inventories may miss important emission sources that are not well documented including emissions from wild fires, volcanic eruptions, and agricultural activities. All these limitations are amplified over the East Asia region because the economic growth in China is so rapid that information needed for bottom-up approach cannot be timely and reliably documented.

To complement information from bottom-up emissions, remote sensing is increasingly used to better quantify aerosol distributions. The satellite observations and/or products can provide information important for the bottom-up estimate of emissions. Examples include the fire products from MODIS, ASTER, and AVHRR sensors that are widely used for characterizing the biomass burning emissions [Borrego et al., 2008; van der Werf et al., 2006; 2010; Reid et al., 2009]. Alternatively, the satellite observed tracer abundance could be used to constrain bottom-up estimates of aerosol emissions through the inverse modeling; such method is referred to as a ‘top-down’ constraint. Although satellite-based aerosol retrievals have less precision than in situ measurements, studies have shown that they are able to quantify the atmospheric aerosol loading and temporal variations with good agreement and expected accuracy to the ground-based observations [Levy et al., 2010; Remer et al., 2005]. Furthermore, the satellite-based aerosol data, in contrast to the ground-based ones, have much higher temporal resolution across the globe. For instance, the MODIS sensor, aboard on NASA’s both Terra and Aqua satellites, has a surface footprint size of about 1 km at nadir and needs only 1 to 2 days to achieve global coverage. In addition, the joint retrieval of aerosols from diverse satellite sensors enhances the accuracy of satellite aerosol

products [Sinyuk et al., 2008], the potential of which have also been shown in the air quality monitoring [Liu et al., 2005; Wang et al., 2010].

Different top-down techniques have been developed to optimally estimates the emissions from satellite observations, which include but are not limited to the following:

- (a) the use of a scaling factor that is the ratio of observed tracer abundances to the CTM simulated counterparts [e.g. Lee et al., 2011; Martin et al., 2003; Wang et al., 2006];
- (b) the use of the local sensitivity of change of tracer concentration to the change of emission [e.g. Lamsal et al., 2011; Walker et al., 2010];
- (c) the analytical Bayesian inversion method [e.g. Heald et al., 2004];
- (d) the adjoint of CTM [e.g. Müller and Stavrakou, 2005; Henze et al., 2007; 2009; Dubovik et al., 2008; Kopacz et al., 2009; 2010; Wang et al., 2012].

The first two methods are similar; both assume a linear relationship between model simulated aerosol abundances and emissions. The analytical method is exact but computationally expensive and thus can only constrain emission in the domain-wise or over coarse spatial resolution [Kopacz et al., 2009]. In contrast to the first three approaches, the adjoint approach is designed for exploiting the high-density of observations to constrain emission with high resolution [Kopacz et al., 2009], as it is able to efficiently calculate gradients of the overall mismatch between observations and model estimates with respect to large sets of parameters (i.e., emissions resolved at each grid box) [Henze et al., 2007].

Several studies have successfully analyzed sources of traces gases using the top-down methods, including CO sources from MOPITT sensor over the Asia [Heald et al., 2004; Kopacz et al., 2009;] and over the globe [e.g. Stavrakou and Müller, 2006; Kopacz et al. 2010], CO₂ surface flux from the TES sensor [Nassar et al., 2011], NO_x emissions

from space-based column NO_2 by several satellite sensors [Lamsal et al., 2011; Lin et al., 2010; Martin et al., 2003; Müller and Stavrou, 2005], and SO_2 from SCIAMACHY and OMI sensors [Lee et al., 2011], etc. However, not all emissions of trace gases can be fully constrained with their satellite-based counterpart products, because some trace gases (e.g. SO_2) can react with other gases (e.g. NH_3), to form either liquid or solid aerosols (e.g. $(\text{NH}_4)_2\text{SO}_4$). As a result, using measurements of trace gases alone can only provide partial constraints on the emission of the corresponding trace gases.

1.1.2 Satellite Observations of Aerosol

Table 1.1: List of satellite sensors with measurement specifications relevant for operation retrieval of aerosol properties.

Sensor	Measurement Specification	Retrieved Aerosol Property	References
AVHRR ^a	15 bands at single view angle	AOD	Dubuisson et al [2009]
CALIOP	Layer backscattering and depolarization ratio	AOD profile	Winker et al [2010]
MERIS	15 bands at single view angle	AOD	Dubuisson et al [2009]

^aFootnotes starts here

1.2 Main Goals of This Work

Based on the preceding discussions, this work aims at improved estimates of global dust emissions through adjoint integration of AOD retrievals from multiple satellite platforms (MODIS and MISR) with a CTM (GEOS-Chem). The overall goal is to conduct the satellite-based global model estimates of atmospheric dust distribution, and thereby advance the understanding of the impacts of atmospheric mineral dust on climate change and air quality. To accomplish this goal, this work pursues the following specific objectives:

- Develop a top-down numerical inversion scheme for constraining global dust emissions with a combined use of multi-platform AOD products and CTM adjoint, which also includes the sensitivity and error budget analysis for the optimization.
- Apply the inversion scheme developed in step 1 for a one year (i.e. 2008) of dust emissions with level 3 quality-controlled MODIS DB and MISR AOD products.
- A long-term (from 2001 to 2010) analysis of dust emissions will follow, along with studies on the seasonal and inter-annual variability of dust emissions, loadings, and direct radiative effects.
- Wherever possible, ground-based and field data will be used to validate and analyze the uncertainties of the inversion results.

Although the adjoint optimization technique we use is similar to that in Dubovik et al. [2008] and Yumimoto et al. [2007], this study differs from the those previous studies in that: (a) Multi-platform AOD products utilized to optimize dust emissions can provide tremendous dust information in fine spatial and temporal scales; (b) This study uses the satellite AOD retrievals only over and near dust source regions where dust has been transported a short distance with minimal influence of precipitation and anthropogenic aerosols; (c) Optimization of the long-term dust emissions is conducted for every grid box as a function of time (e.g., on the weekly or month scale). Although the criteria for separation of a natural and anthropogenic dust source is not clear and sometime controversial in the literature [Denman et al., 2007], especially when considering the climatic feedback on dust emissions [Zhang et al., 2002], we believe that satellite-based optimization of global dust emissions in the last decade could improve our modeling of dust radiative forcing and potentially illuminate anthropogenic components of dust sources and loadings, currently estimated at

0-20% though values as large as 50% has been postulated [Ginoux et al., 2011; Tegen et al., 1996; 2004; Mahowald et al., 2004,].

1.3 Organization of This Dissertation

We describe the GEOS-Chem simulation of mineral dust in Chapter 2 with emphasizing the physical parameterization of dust sources, after which we present the implements for the AOD observation operator and the adjoint capacity of dust emission within the GEOS-Chem adjoint model in Chapter 3. In chapter 4, we present a case study on optimizing the dust emission estimates from the satellite (MODIS) radiances over the eastern Asia, in which we also attempt to simultaneously constrain the anthropogenic emissions of the SO_2 , NO_2 , NH_3 , and carbaceous aerosols together with the dust aerosols. In chapter 5, we optimize the dust source parameterization from multi-satellite AOD products, particularly in improving the the estimates of soil erodibility and wind friction threshold for sand saltation over the northern Africa. Finally, we summarize the dissertation and outlook future work in Chapter 6.

CHAPTER 2

TOP-DOWN INVERSION FRAMEWORK

Overview Mathematically, solving an inverse problem involves two types of development, i.e., the forward modeling and inverse modeling. This chapter presents how the physical process that mineral dust involved are quantitatively represented in a chemistry transport model, i.e., the GEOS-Chem model. These processes include the uplifting of dust from soil surface, the transport within the atmosphere, and deposition of dust to the surface.

2.1 Inversion Theory and Infrastructure

Let \mathbf{x} denote a state vector of n parameters to be constrained and \mathbf{y} an observation vector assembled by m measurements, and let \mathbf{F} indicate a forward model that describes the physics of the measurement process. Then, we can express the relationship between the observation vector and the state vector as

$$\mathbf{y} = \mathbf{F}(\mathbf{x}) + \boldsymbol{\epsilon}, \quad (2.1)$$

where $\boldsymbol{\epsilon}$ is an experimental error term that includes observation noise and forward modeling uncertainty.

For this work, the observation vector \mathbf{y} comprises measurements of aerosol loading, such as mass concentrations or optical depth, at any temporal and spatial scale. The components of the state vector \mathbf{x} could vary according to our inversion focus. For the inversion of aerosol

emission estimates (as in the Chapter ??), \mathbf{x} comprises the emission fluxes (or their scaling factors) of defined aerosol species within each grid cell of specified temporal resolution. In contrast, \mathbf{x} consists of dust emitting parameters (or their scaling factors) when we tend to constrain the dust emission parameterization (as in the Chapter 4). The forward model \mathbf{F} represents the GEOS-Chem that maps parameters from the state space to the observation space. The inversion of the state vector from these measurements is often an ill-posed problem due to non-linearity and limited sensitivity of these observed quantities to the constrained parameters. We need to combine additional constraints to make the problem amenable to inversion.

A priori information describes our knowledge of the state vector before measurements are applied. *A priori* constraint is commonly used to achieve a well-defined stable and physically reasonable solution to an ill-posed problem. Usually, *a priori* knowledge comprises both a mean state \mathbf{x}_a and its error ϵ_a :

$$\mathbf{x} = \mathbf{x}_a + \epsilon_a \quad (2.2)$$

Under assumption of Gaussian-distributed errors, the Maximum A Posteriori solution of equations (2.1) and (2.2) according to the Bayesian approach corresponds to the state vector that minimizes the quadratic cost function [Rodgers, 2000]:

$$J(\mathbf{x}) = \frac{1}{2} [\mathbf{F}(\mathbf{x}) - \mathbf{y}]^T \mathbf{S}_y^{-1} [\mathbf{F}(\mathbf{x}) - \mathbf{y}] + \frac{1}{2} \gamma (\mathbf{x} - \mathbf{x}_a)^T \mathbf{S}_a^{-1} (\mathbf{x} - \mathbf{x}_a), \quad (2.3)$$

where T indicates the transpose operation, \mathbf{S}_y is the error covariance matrix of measurements, \mathbf{S}_a is the error covariance matrix of the *a priori*, and γ is the regularization parameter. These two terms on the right side of equation (2.3) represent the total squared fitting error incurred owing to departures of model predictions from the observations and the penalty error

incurred owing to depatures of the estimates from the *a priori*, respectively. Thus, the minimization of $J(\mathbf{x})$ achieves the objectives of improving the agreement between the model and the measurements while ensuring that the solution remains within a reasonable range and degree of smoothness.

The regularization parameter γ in the calculation of $J(\mathbf{x})$ acts weights to balance the fitting error and the penalty error. Clearly, a good assignment of γ is of crucial importance for the statistically optimal solution. High values of γ can lead to over-smoothing of the solution with little improvement to the fitting residuals, while low values minimize the error term at the cost of greatly increasing the penalty term. Optimal values of γ can be identified at the corner of the so-called L-curve [[Hansen, 1998](#)].

In principle, solving this inverse problem is tantamount to a pure mathematical minimization procedure. The minimization of $J(\mathbf{x})$ is performed with an iterative quasi-Newton optimization approach using the L-BFGS-B algorithm [[Byrd et al., 1995](#); [Zhu et al., 1994](#)], which offers bounded minimization to ensure the solution stays within a physically reasonable range. The L-BFGS-B algorithm requires knowledge of \mathbf{x} and $J(\mathbf{x})$, as well as the gradient of $J(\mathbf{x})$ with respect to \mathbf{x} , $\Delta_{\mathbf{x}}J$. By linearizing the forward model $F(\mathbf{x})$, we can determine $\Delta_{\mathbf{x}}J$ by

$$\Delta_{\mathbf{x}}J = \mathbf{K}^T \mathbf{S}_y^{-1} [\mathbf{F}(\mathbf{x}) - \mathbf{y}] + \gamma \mathbf{S}_a^{-1} (\mathbf{x} - \mathbf{x}_a), \quad (2.4)$$

where \mathbf{K} is the Jacobian matrix of $\mathbf{F}(\mathbf{x})$ with respect to \mathbf{x} , which is computed analytically by adjoint method in the GEOS-Chem adjoint. At each iteration, improved estimates of the state vector are implemented and the forward simulation is recalculated. The convergence criterion to determine the optimal solution is the smallness of the $J(\mathbf{x})$ reduction and the norm of $\Delta_{\mathbf{x}}J$. The iteration stops when the reduction of $J(\mathbf{x})$ is less than 1% within five continuous iterations. Then, the optimal solutions are identified corresponding to the smallest norm of $\Delta_{\mathbf{x}}J$ among these five last iterations.

2.2 GEOS-Chem Forward Modeling

The GEOS-Chem chemistry transport model is used to simulate the ambient concentrations of atmospheric aerosols.

The GEOS-Chem aerosol simulation was based on the GOCART model [Chin et al., 2002], particularly for wet scavenging, with updates described by Park et al. [2004].

Particularly for the interest of this study

2.2.1 Anthropogenic aerosol emissions

2.2.2 Dust emissions

The dust emission, aerolian wind erosion that results in production of mineral aerosols from soil grains, involves complex and nonlinear processes that are governed by the meteorology as well as by the state and properties of the land surfaces. Laboratory [Iversen and White, 1982] and field [Shao et al., 1996; Zender et al., 2003] wind tunnel studies suggested that dust is primarily injected into the atmosphere during the sandblasting caused by the saltation bombardment [Alfaro and Gomes, 2001; Grini et al., 2002]. The clay- and silt-sized soil particles have strong inter-cohesive force... The saltation of sand-sized particles ... requires least threshold of wind speed...

The most important factors include wind friction velocity and its threshold for saltation, vegetation cover, soil minerology, and surface soil moisture.

In this study, the physical parameterization of dust emission is taken from a Dust Entrainment and Deposition (DEAD) model developed by Zender et al [2003a]. The DEAD scheme calculates the wind friction threshold (u_{*t}) as a function of the Reynolds number following Iversen and White [1982] and Marticorena and Bergametti [1995]. Three processes are also considered to modify the u_{*t} : the drag partitioning owing to the momentum captured

by nonerodible roughness elements, the Owen effect, and moisture inhibition. The horizontal saltation flux (Q_s) that is defined as the vertical integral of the stream-wise soil flux density is calculated following the theory of White [1979]:

$$Q_s(u_*, u_{*t}) = \frac{c_s \rho}{g} u_*^3 \left(1 - \frac{u_{*t}}{u_*}\right) \left(1 + \frac{u_{*t}}{u_*}\right)^2, \quad (2.5)$$

where, $c_s = 2.61$, ρ is the air density at surface level, and u_* is the wind friction velocity. Thus, it assumes the saltation flux is quasi-linearly the u_*^3 when u_* exceeds the u_{*t} . It also neglect the dependence of total Q_s on the soil size.

the total vertical mass flux of dust into transport bin j is

$$E_{d,j} = \begin{cases} T_0 A_m S \alpha Q_s \sum_{i=1}^3 M_{i,j} & \text{if } u_* \geq u_{*t}, \\ 0 & \text{if } u_* < u_{*t}, \end{cases} \quad (2.6)$$

where, T_0 is a tuning factor chosen to adjust the global amount, A_m is the fraction of bare soil exposed in a model grid cell, S is called "erodibility" or "preferential source function", α is the sandblasting mass efficiency factor which depends on the mass fraction of clay particles in the parent soil, and $M_{i,j}$ indicates the mass fraction of i th source mode carried into the j th transport mode.

2.3 GEOS-Chem Adjoint Modeling

The adjoint of the GEOS-Chem model was developed specifically for inverse modeling of aerosol (or their precursors) and gas emissions [Henze *et al.*, 2007, 2009], and it is continuously improved and maintained by the GEOS-Chem Adjoint and Data Assimilation Working Group and its users (<http://wiki.seas.harvard.edu/geos-chem/index>).

[php/GEOS-Chem_Adjoint](#)). The strength of the adjoint model is its ability to efficiently calculate model sensitivities with respect to large sets of model parameters, such as aerosol emissions at each grid box. These sensitivities can serve as the gradients needed for inverse modeling of aerosol emissions. Recent studies have used the GEOS-Chem adjoint with satellite observations to constrain sources of species such as CO [*Kopacz et al.*, 2009, 2010; *Jiang et al.*, 2011], CH₄ [*Wecht et al.*, 2012], and O₃ [*Parrington et al.*, 2012] to diagnose source regions for long-range transport [*Henze et al.*, 2009; *Kopacz et al.*, 2011], and to provide guidance on future geostationary observations of surface air quality [*Zoogman et al.*, 2011].

CHAPTER 3

OPTIMIZING SPECIES-SPECIFIED AEROSOL EMISSIONS

3.1 Introduction

In this chapter, we present a new attempt for the top-down estimate of aerosol emissions through integration of the satellite observation of reflectance and GEOS-Chem Adjoint model. The technique is applied to improve estimates of mineral dust and anthropogenic SO_2 , NH_3 , NO_x , BC and OC emissions over China for April 2008, during which ground-based PM_{10} (particulate matter with aerodynamic diameter of $10\text{ }\mu\text{m}$ or less) data is available from a joint China-U.S. dust field experiment [Huang et al., 2010]. This paper differs from the past work in that: (i) satellite reflectance (in essence radiance) is used to constrain the emission estimates of aerosol particle and precursors, which eliminates the discrepancy of aerosol optical properties between model simulated and satellite retrieved AOD; (ii) we use a suite of aerosol and gas measurements from satellite sensors and ground-based instruments to independently evaluate our results, and test our hypothesis that temporal variation of AOD at different locations, as characterized by satellite observations, can be a strong constraint for species-specific source estimates if they are combined with the model-based knowledge of the dominant aerosol sources and the source-receptor relationship at corresponding locations; and (iii) combination of (i) and (ii) will provide the basis and a necessary step forward for future research to simultaneously use both gas and AOD measurements to constrain speciated aerosol emissions.

We describe the top-down inversion scheme and its key components (i.e., GEOS-Chem forward model and its adjoint, and observational constraints) in Section 2. The top-down constraints on aerosol emissions over China for the period of April 2008 are presented in Section 3, and evaluated in Section 4. Interpretation and implications of the results are discussed in Section 5, and Section 6 summaries this study. [needs updates!!!!]

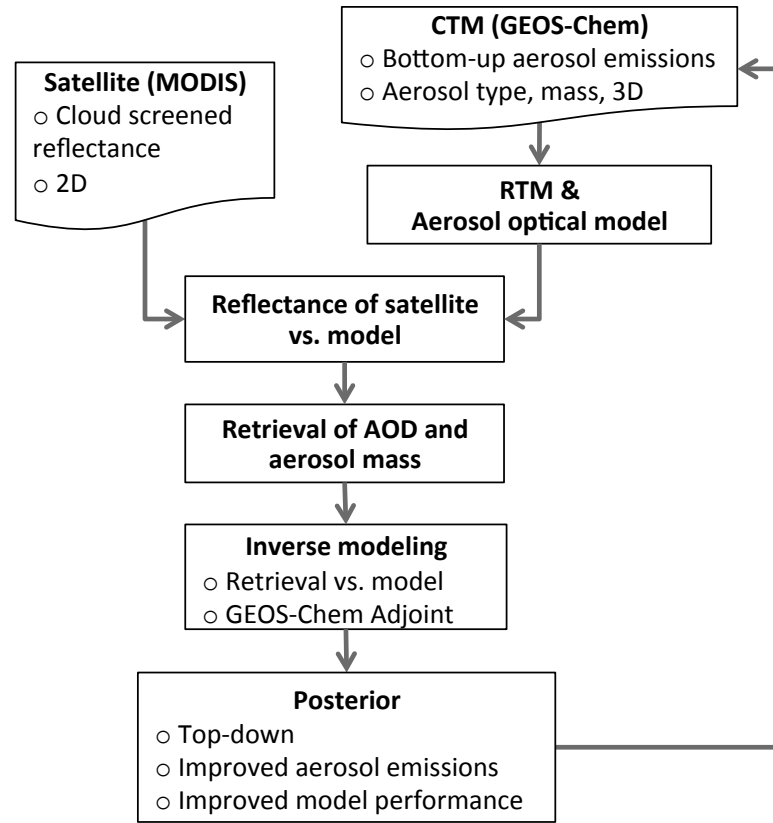


Figure 3.1: Flowchart of the proposed top-down inversion framework.

As shown in Figure 3.1, the top-down inversion approach in this study integrates the MODIS radiance/reflectance with the GEOS-Chem (section 2.1) and its adjoint model (section 2.2) to optimize aerosol emissions. First, similar to Wang et al. [2010], we retrieve the atmospheric aerosol mass and AOD through fitting the calculated radiance based on GEOS-Chem aerosol composition and single optical properties to the MODIS cloud-free

radiance (section 2.3). Second, the retrieved AOD (hereafter retrieved MODIS AOD) from the first step is used as an observational constraint to optimize the aerosol emissions by inverting the GEOS-Chem chemical transport model (section 2.4). The approach aims to improve aerosol emission estimates that ultimately will yield better agreement between model simulated and satellite-observed reflectances. Since the aerosol single scattering properties are exactly the same between the retrieval algorithm and GEOS-Chem (as done in the first step), the top-down inversion scheme essentially uses the MODIS radiances (in the form of retrieved AOD) to scale the GEOS-Chem aerosol mass, which in turn are used to optimally adjust the aerosol emissions. The approach here is first demonstrated through a pseudo-observation experiment (Section 2.5) before it is applied to real observations (Section 3).

3.2 Constraints from Satellite Radiances

3.3 Selection of Emissions for Optimization and Sensitivity Tests

3.4 Inversion Results

3.5 Results Evaluations

3.6 Implications of Results

3.7 Summary

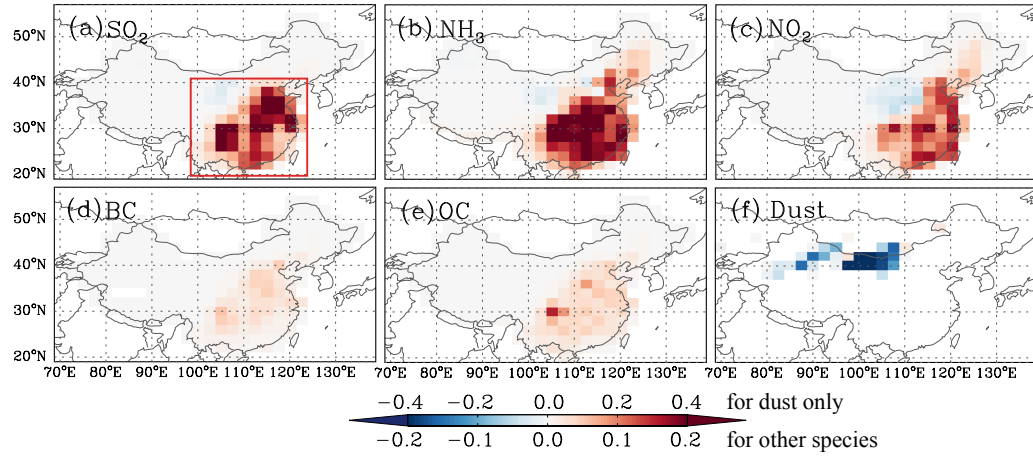


Figure 3.2: Relative changes in posterior aerosol emissions from *a priori* in the pseudo-observation experiment. Six panels are respectively for anthropogenic emissions of SO_2 , NH_3 , NO_x , BC, and OC, and mineral dust from both natural and anthropogenic sources. The red box in panel (a) indicates the region where AOD observations are selected.

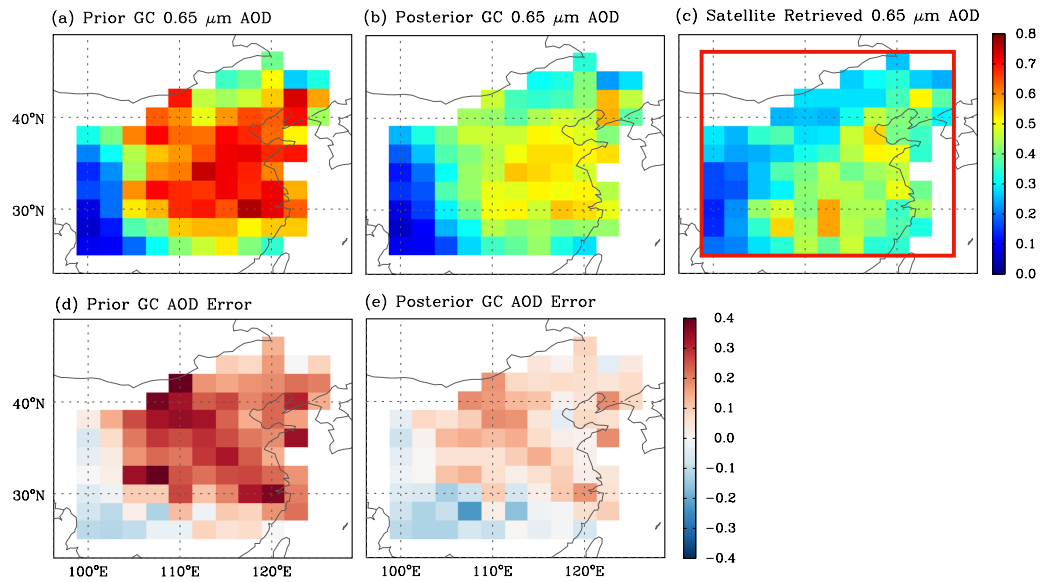


Figure 3.3: Comparison of the prior (a) and posterior (b) GEOS-Chem (GC) simulation of $0.65 \mu\text{m}$ AOD with the AOD at the same wavelength retrieved from MODIS reflectance using GEOS-Chem aerosol optical properties (c) averaged for the period of April 2008. Satellite retrievals with 10 km by 10 km at nadir are aggregated to GEOS-Chem grid cells; and the model AOD are sampled coincidentally with those retrievals. Panel (d) and (e) respectively show the difference of prior and posterior simulated from the satellite retrieved AODs. The red box in panel (c) indicates the region where AOD observations are selected.

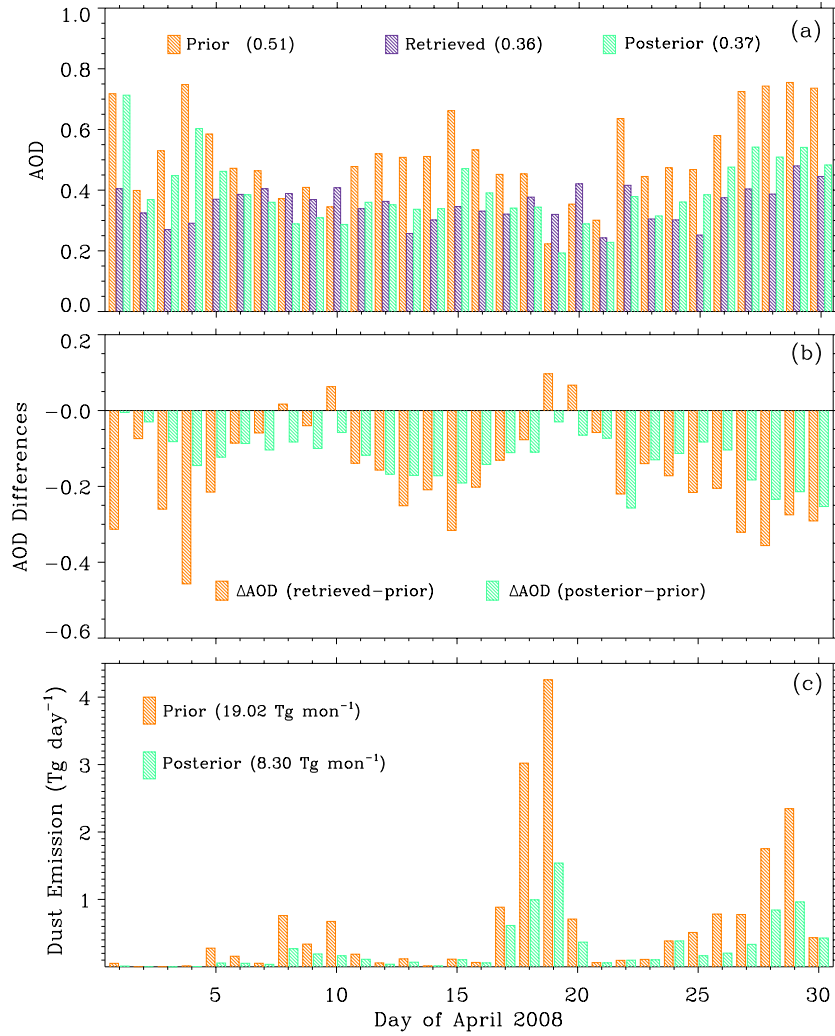


Figure 3.4: (a) Time series of the spatially averaged daily MODIS AOD retrievals (purple) for April 2008 over the Eastern China, compared by the prior (orange) and posterior (green) spatial averaged daily GEOS-Chem AOD that are sampled in the MODIS AOD temporal-spatial space. (b) Time series of the expected daily AOD adjustments (orange) that are the differences between MODIS AOD and the prior GEOS-Chem AOD and their real adjustments (green) that are the differences of posterior from prior GEOS-Chem AOD. (c) Time series of the prior (orange) and posterior (green) daily dust emissions over China for April 2008.

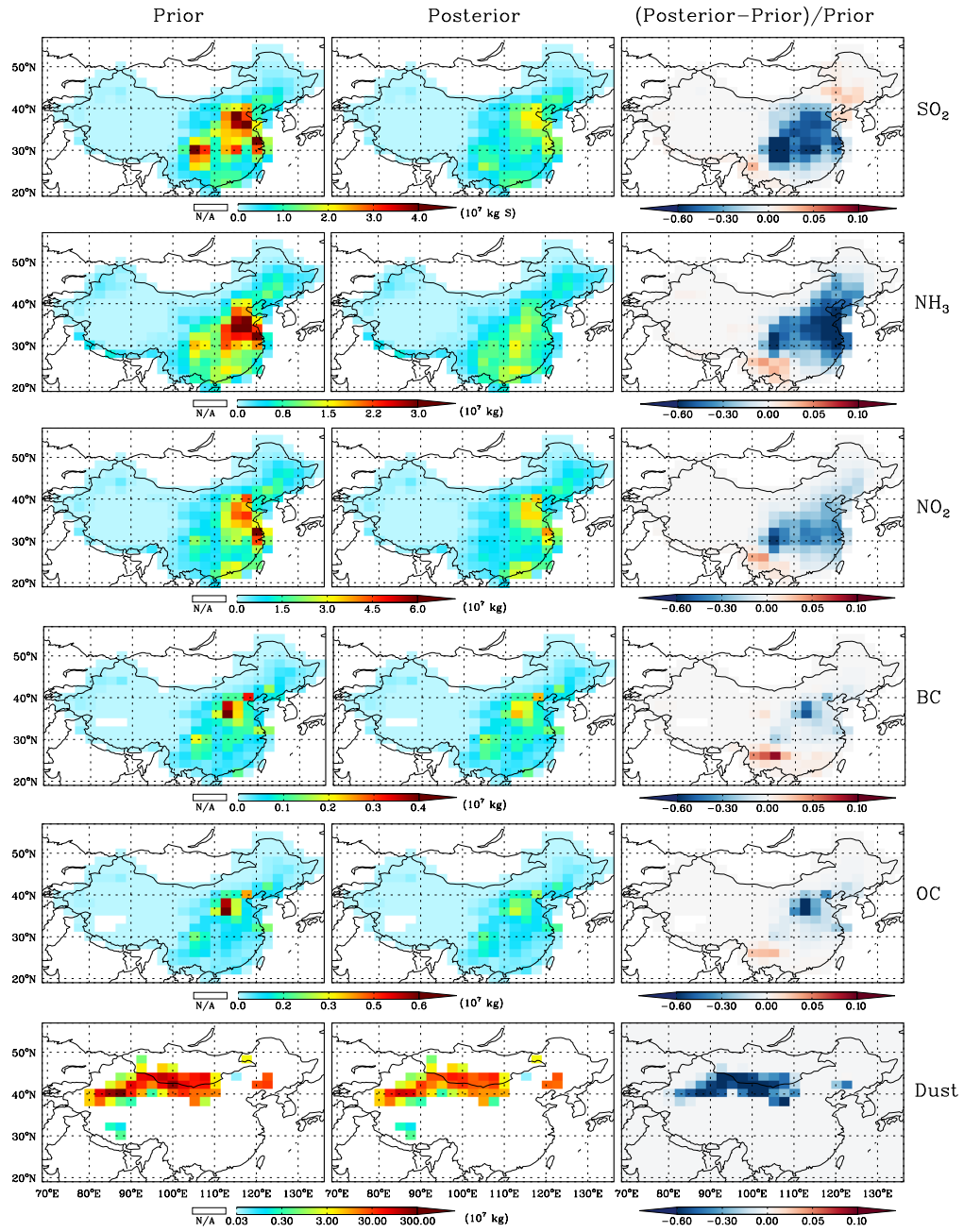


Figure 3.5: The prior (or bottom-up based, left column), optimized (or top-down constrained, middle column) aerosol emissions over China for the period of April 2008, and their relative differences (right column). Six rows from top to bottom are respectively for anthropogenic emissions of SO_2 , NH_3 , ceNO_x , BC, and OC, and mineral dust from both natural and anthropogenic sources.

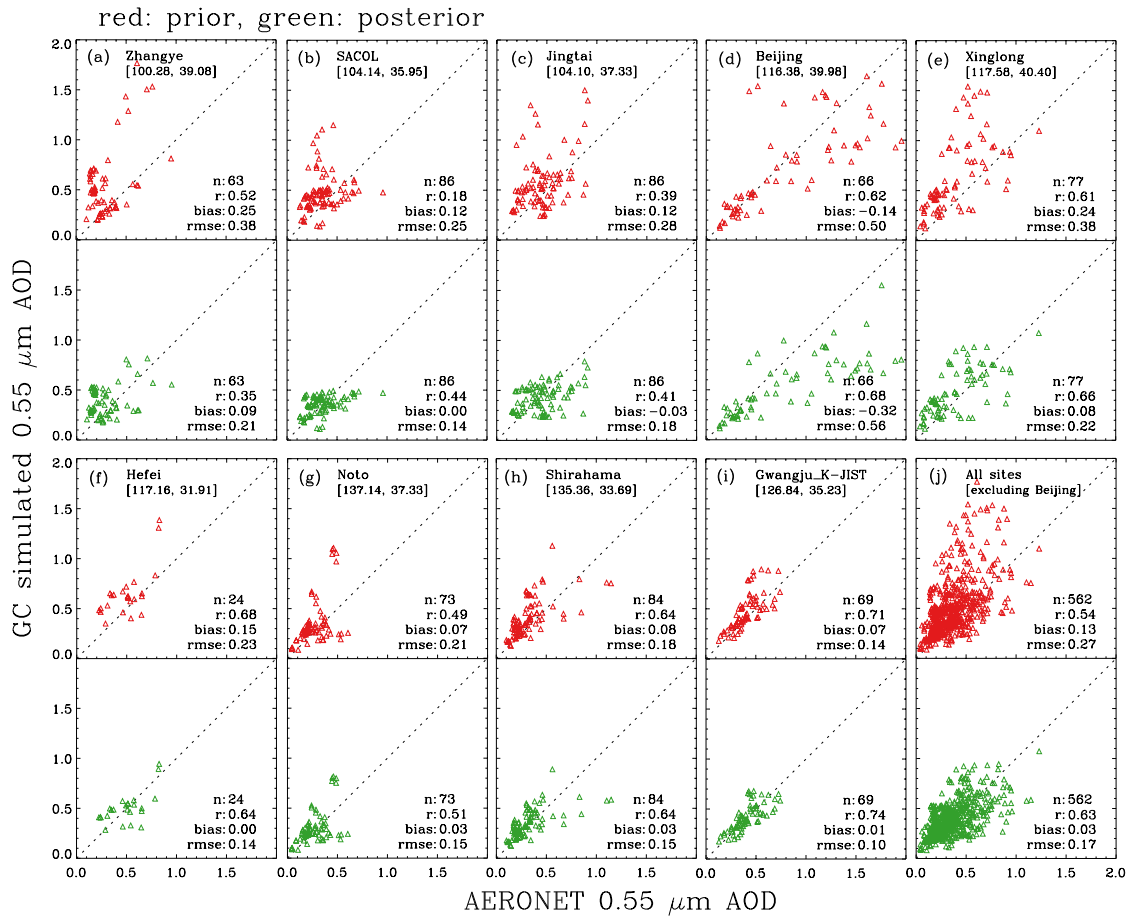


Figure 3.6: (a – i) Scatterplots of GEOS-Chem AOD versus AERONET AOD at $0.55 \mu\text{m}$ prior (red scatters) and posterior (green scatters) to the aerosol emission optimization over nine stations. AERONET AODs are 3-hour averages following the GEOS-Chem output frequency. (j) The overall comparison for eight AERONET sites excluding Beijing. Also shown are the number of valid sampled pairs (n), correlation coefficients (R), bias, and root-mean-square-error (rmse).

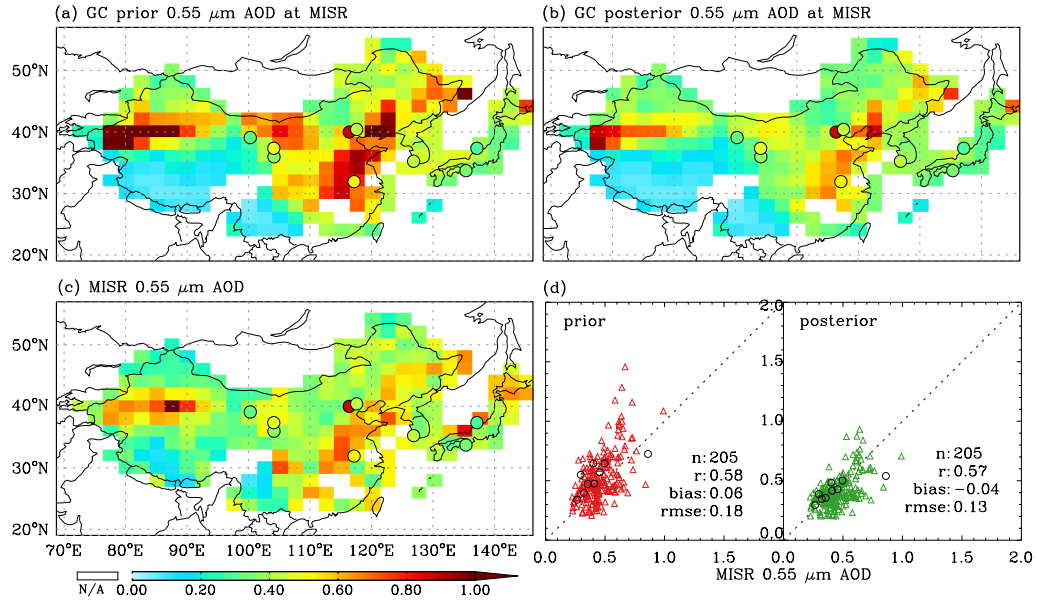


Figure 3.7: Comparison of the prior and posterior GEOS-Chem simulation of $0.55 \mu\text{m}$ AOD with the level 3 MISR $0.55 \mu\text{m}$ AOD for the period April 2008. (a) The prior GEOS-Chem $0.55 \mu\text{m}$ AOD that are sampled coincidentally with MISR AODs for the period of April 2008. Also overlaid circles are the monthly AOD averages at $0.55 \mu\text{m}$ observed from the nine AEORNET sites shown in Figure 3.6. (b) Same as (a) but for the monthly average of posterior GEOS-Chem AOD. (c) Monthly average of the Level 3 daily MISR $0.55 \mu\text{m}$ AOD. (d) Scatter plot the GEOS-Chem AOD versus the MISR AOD before (red scatters) and after optimization (green scatters), in which each point indicates an AOD pair over a model grid cell with value over 0.2. Also shown are the statistics including number of sampled pairs (n), correlation coefficient (R), bias and root-mean-square-error (rmse). Comparisons of the monthly GEOS-Chem AOD versus AERONET AOD are also included as the black circles; each circle indicates an AOD pair over an individual site.

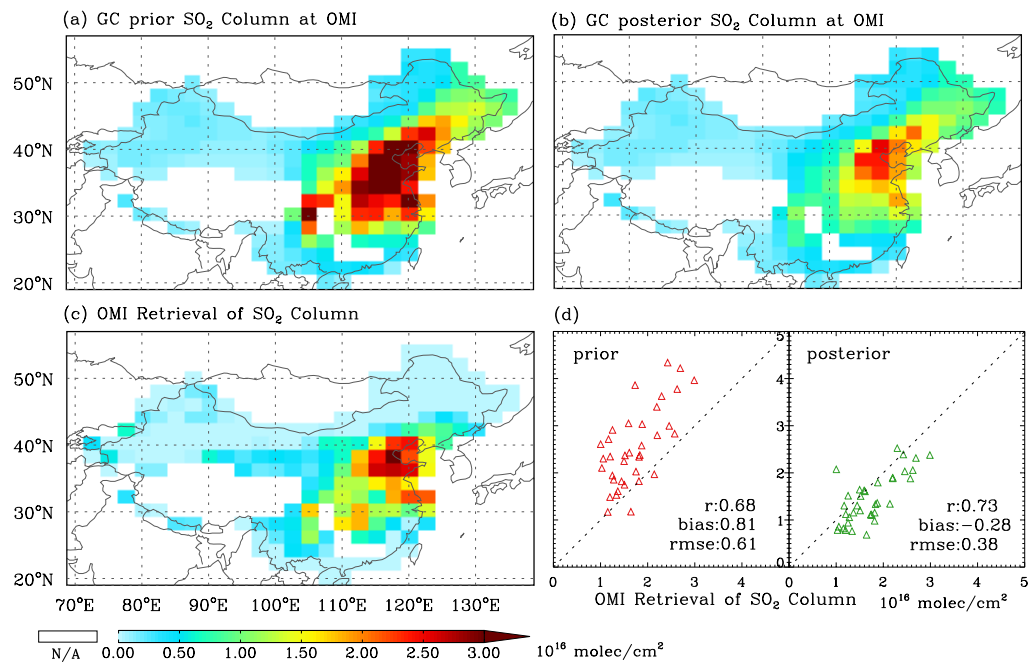


Figure 3.8: Same as figure 3.7 but for comparison of the GEOS-Chem SO₂ simulation with OMI column SO₂ retrievals for the period of April 2008. The OMI planetary boundary layer (PBL) column SO₂ from the Level 3 daily products with 0.25° by 0.25° resolutions are aggregated into GEOS-Chem grid cells.

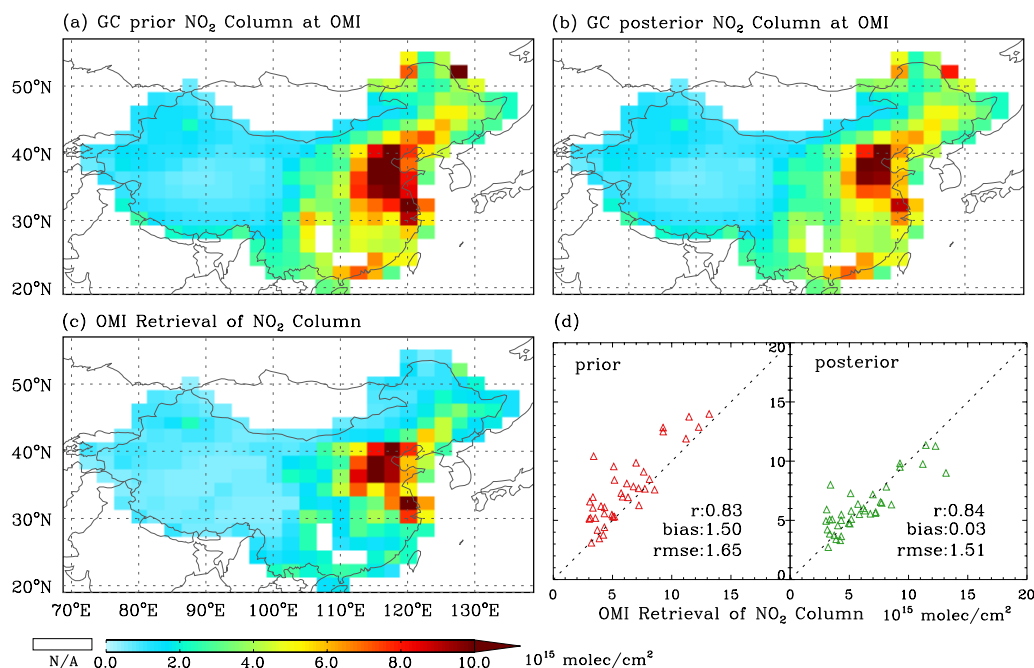


Figure 3.9: Same figure 3.7 but for comparison of the GEOS-Chem NO₂ simulation with OMI column NO₂ retrievals for the period of April 2008. The OMI tropospheric column NO₂ from Level 2 daily products with 0.25° by 0.25° resolutions are aggregated into GEOS-Chem grid cells.

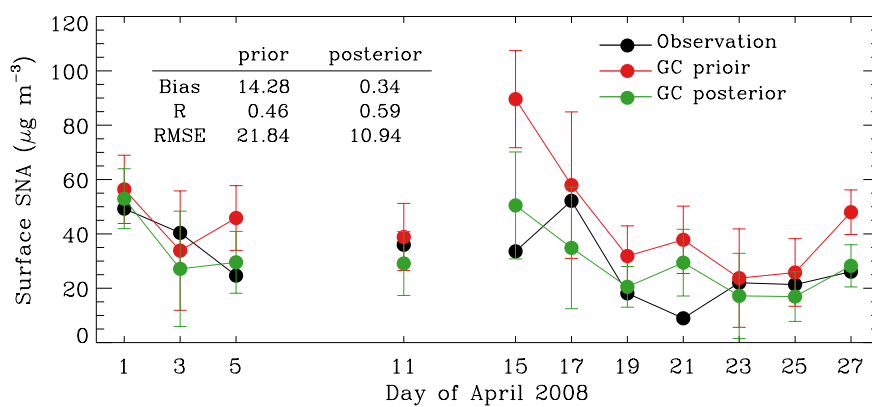


Figure 3.10: Comparison of the GEOS-Chem surface mass concentration of sulfate-nitrate-ammonium (SNA) aerosols with ground-based observations over Qingdao (120.34° E, 36.06° N), China. Discontinuity in time series is due to missing or quality filtered observations.

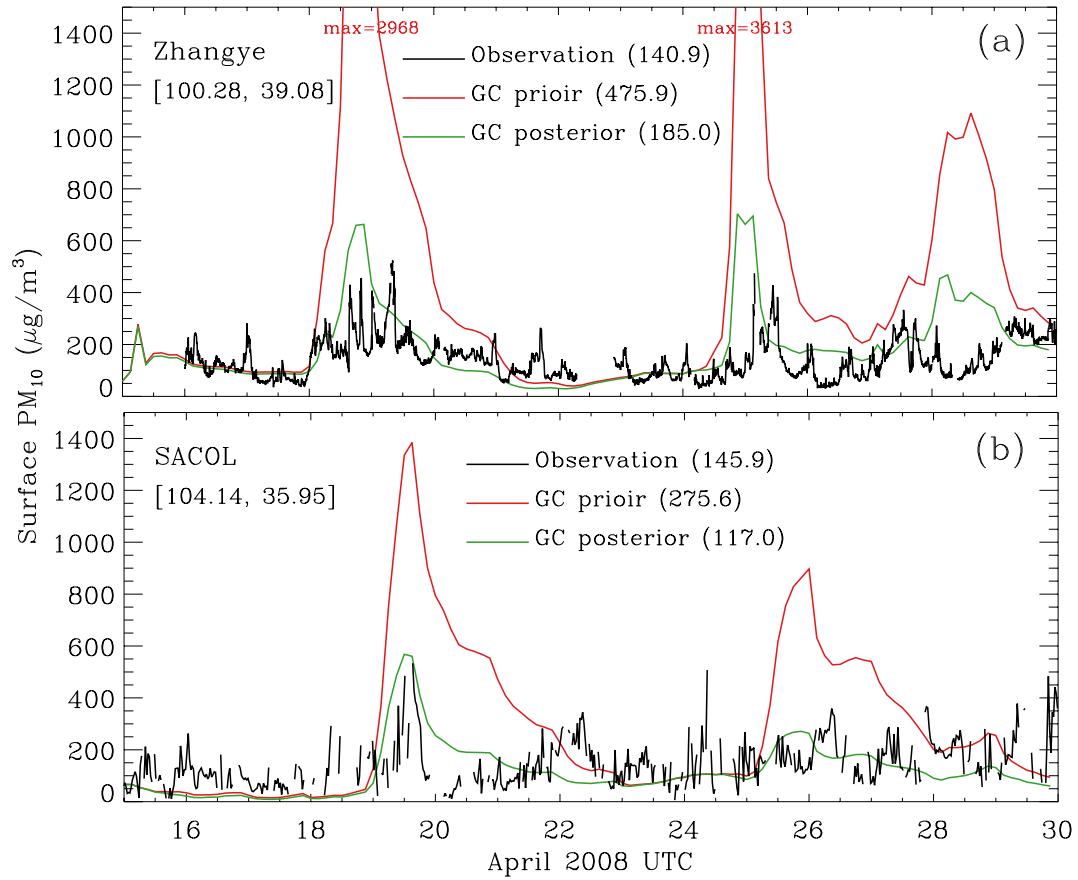


Figure 3.11: Time serial plot of the GEOS-Chem simulated surface PM_{10} concentrations by prior (red) and posterior (red) aerosol emissions compared with the *in situ* measured PM_{10} (black) over Zhangye (a) and SACOL (b) stations for 15 – 30 April 2008; also shown are the average values over same the period. Discontinuity in time series is due to missing or quality filtered observations.

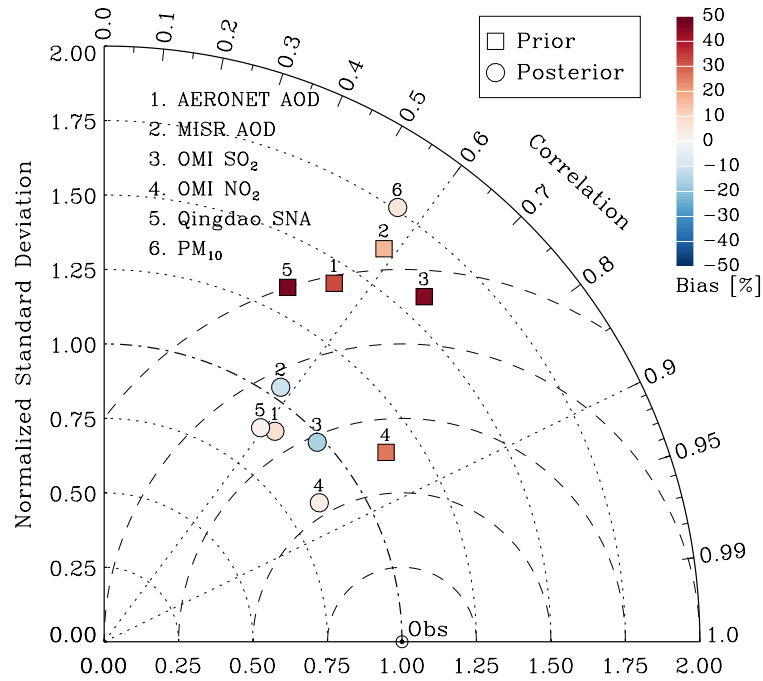


Figure 3.12: Taylor diagram for the model evaluations before (squares) and after (circles) optimization when comparing against (1) AERONET AOD at $0.55 \mu\text{m}$, (2) MISR $0.55 \mu\text{m}$ AOD, (3) OMI column SO₂, (4) OMI column NO₂, (5) surface SNA concentrations at Qingdao site, and (6) surface PM₁₀ concentrations measured at Zhangye and SACOL sites. The color coded on each point indicates the relative bias. It should be noted that the ratio of standard deviations and correlation coefficient between prior GEOS-Chem simulated and measured surface PM₁₀ over Zhangye and SACOL are 6.5 and 0.45, which makes the point number 6 for the prior simulation far beyond the range of this Taylor diagram.

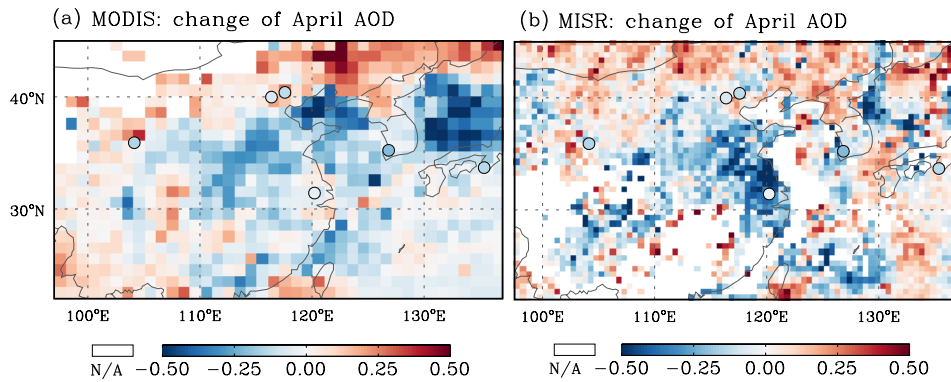


Figure 3.13: Change of April monthly $0.55 \mu\text{m}$ AOD from 2006 to 2008 from MODIS (a) and MISR (b) Level 3 daily products.

CHAPTER 4

OPTIMIZING DUST SOURCE PARAMETERIZATION

4.1 Introduction

Mineral dust accounts for about 40% of the global annual emissions of tropospheric aerosols [Textor *et al.*, 2006; Boucher *et al.*, 2013]. Naturally, these mineral particles are uplifted mainly by the aerolian wind erosion in arid and semiarid areas. Anthropogenic sources of mineral aerosols include road dust and mineral dust due to land changes by human activities [Tegen *et al.*, 1996, 2004; Ginoux *et al.*, 2012]. In the atmosphere, mineral dust can be transported thousands of miles away from its sources [Husar *et al.*, 2001; Toon, 2003] and influences many aspects of the Earth system through its interactions with atmospheric chemistry, solar and terrestrial radiation, clouds, and biosphere [Shao *et al.*, 2011; Ravi *et al.*, 2011; Satheesh and Krishna Moorthy, 2005; Carslaw *et al.*, 2010]. An accurate representation of dust cycle in the Earth climate model is thus critical to assess these impacts. However, significant uncertainties prevail in quantifying mineral dust sources due to the limited understanding of dust uplifting mechanisms and the lack of in situ measurements over the desert region.

Parameterization of dust entrainments in a chemistry transport model (CTM) requires knowledge of many parameters that are poorly characterized, including surface wind speed, soil moisture, soil texture, and surface state and roughness [Tegen and Fung, 1994; Ginoux *et al.*, 2001; Zender *et al.*, 2003]. Not surprisingly, recent estimates of global annual dust

emissions in CTMs span from a few hundreds to over 4000 Tg [Huneus *et al.*, 2011] and can vary by a factor as large as fifteen at regional scales for the same dust event(s) [Uno *et al.*, 2006]. An observation-based approach, therefore, is needed to reduce these large uncertainties in estimate of dust emissions and further improve the global modeling of atmospheric dust distribution and their impacts.

In the last decade, the *in situ* and satellite remote sensing observations have greatly enhanced our understanding of the spatiotemporal variations and radiative effects of dust aerosol. This is especially true for satellite retrievals that are based on multi-spectral and multi-angle radiance measurements from NASA’s Earth Observing System satellite instruments, such as MODIS and MISR, which provide daily information of aerosol optical depth (AOD) across the globe [King *et al.*, 1999; Kaufman *et al.*, 2002; Martonchik *et al.*, 2009]. The MODIS “deep blue” (DB) aerosol retrievals [Hsu *et al.*, 2006, 2013] further made the aerosol information over bright deserts available. On the other hand, *in situ* observations (e.g. AERONET [Holben *et al.*, 1998]) and experiment campaigns, even though sparse in their temporal and spatial coverage, usually have advantages in their accuracy, and thus are valuable for validating satellite aerosol products and model simulations.

In this dissertation, I thus seek to contribute an improved understanding of the dust emissions through (i) . . . , (ii) . . . , and (iii).

4.2 Necessary Implementations

4.2.1 Development of the wind speed distribution

In order to incorporate the variability of wind speed due to the subgrid scale circulations, we introduce a probability density function (PDF) of the wind speed within each grid box. The dust emission is computed according to the fraction of the PDF that exceeds the threshold

value:

$$E_d = \int_{u_{*l}}^{\infty} E(u_*) p(u_*) du_*. \quad (4.1)$$

Where $E(u_*)$ is the emission as a function of the surface wind friction velocity, and $p(u_*)$ is the PDF of u_* within the grid box.

The PDF for surface wind speeds can be represented by a Weibull distribution [Justus et al., 1978] and has been used in recent studies [e.g., Grini and Zender, 2004; Grini et al., 2005; Ridley et al., 2013] to characterize the subgrid dust emissions. The PDF of a Weibull random variable x is described by a shape factor k and a scale factor c :

$$p(x; c, k) = \frac{k}{c} (x/c)^{k-1} \exp \left[-(x/c)^k \right], \text{ for } x > 0. \quad (4.2)$$

One of the advantages in using the Weibull PDF is that it is analytically integrable with the cumulative distribution function:

$$P(x \leq x_1; c, k) = 1 - \exp \left[-(x/c)^k \right]. \quad (4.3)$$

Based on above cumulative function, we cut off wind speeds with a minimum and a maximum wind speed to retain the central 98% of the wind PDF. As a result, the lower and upper limits of wind speed are respectively:

$$x_l = c \left[-\ln 0.99 \right]^{\frac{1}{k}} \quad (4.4)$$

$$x_u = c \left[-\ln 0.01 \right]^{\frac{1}{k}} \quad (4.5)$$

Parameters k and c can be estimated from the statistical mean \bar{x} and variance σ^2 (of x),

since they are related to \bar{x} and σ^2 :

$$\bar{x} = c\Gamma(1 + 1/k) \quad (4.6)$$

$$\sigma^2 = c^2 [\Gamma(1 + 2/k) - \Gamma^2(1 + 1/k)] \quad (4.7)$$

Where $\Gamma()$ is a gamma function. According to Justus et al. [1978], k and c can be best estimated by:

$$k = (\sigma/\bar{x})^{-1.086} \quad (4.8)$$

$$c = \bar{x}[\Gamma(1 + 1/k)]^{-1} \quad (4.9)$$

Thus, the only parameter that must be supplied beyond the mean wind speed is the variance (σ^2) of subgrid wind speeds within the grid box. Cakmur et al [2004] calculated the σ^2 by incorporating information from the parameterizations of the planetary boundary layer along with dry and moist convection. Here, we follow Grini and Zender [2004] and Grini et al [2005] that assumed an approximation of k based on Justus et al. [1978]:

$$k = 0.94u_*^{\frac{1}{2}} \quad (4.10)$$

Finally, the dust emission flux is calculated by

$$E_{d,j} = A_m S \alpha \left(\sum_{i=1}^3 M_{i,j} \right) \frac{c_s \rho}{g} \int_{u_{*t}}^{u_{*u}} u_*^b \left(1 - \frac{u_{*t}}{u_*} \right) \left(1 + \frac{u_{*t}}{u_*} \right)^2 p(u_*) du_*. \quad (4.11)$$

Where u_{*u} is the upper limit of wind speed determined by equation (4.5).

4.2.2 AOD observation operator

Inversion of dust emissions from AOD observations requires an observation operator that relates AOD to emission. Such observation operator of this study comprises a GEOS-Chem forward model that simulates aerosol concentrations with input of emissions and an AOD operator that computes AOD from aerosol concentrations. AOD at any wavelength is calculated from the sum of AODs of each component assuming external mixing state of aerosol particles:

$$\tau_A = \sum_{i=1}^{n_{\text{spec}}} \beta_{\text{ext}_i} c_i \frac{3c_i Q_{\text{ext}_i}}{4\rho_i r_{\text{eff}_i}} \quad (4.12)$$

where n_{spec} is the number of aerosol components, c_i is the aerosol mass concentration of the i th component, and β_{ext_i} is the mass extinction efficiency. β_{ext_i} is related to the

4.2.3 Adjoint for Dust Flux Parameterization

In simple, The dust emission flux considering subgrid wind speeds in equation (4.11) can be written

$$E_{d,j} = C_j S' \int_{u_{*t}}^{u_{*u}} Q_s(u_*, u_{*t}, b) p(u_*) du_*, \quad (4.13)$$

where $S' = S\alpha$, and $C_j = A_m \sum_{i=1}^3 M_{i,j}$. We combine the erodibility S and sandblasting factor α , because both of them not only are related to the soil texture but also describe the strength efficiency of dust emission. Given the the state of land surface and the properties of surface soil, the dust emission is a function of S' , b , and u_{*t} .

Here we implement the adjoint calculation for three parameters, i.e., S' , b , and u_{*t} . This implementation requires the partial derivatives of $E_{d,j}$ with respect to these parameters (when $u_* \geq u_{*t}$):

$$\frac{\partial E_{d,j}}{\partial S'} = \frac{E_{d,j}}{S'}, \quad (4.14)$$

$$\frac{\partial E_{d,j}}{\partial b} = C_j S' \int_{u_{*t}}^{u_{*u}} \frac{\partial Q_s}{\partial b} p(u_*) du_*, \quad (4.15)$$

$$\frac{\partial E_{d,j}}{\partial u_{*t}} = C_j S' \int_{u_{*t}}^{u_{*u}} \frac{\partial Q_s}{\partial u_{*t}} p(u_*) du_*. \quad (4.16)$$

These gradients of Q_s in equations (4.15 and 4.16) can be calculated by

$$\frac{\partial Q_s}{\partial b} = Q_s(u_*, u_{*t}, b) \ln u_* \quad (4.17)$$

$$\frac{\partial Q_s}{\partial u_{*t}} = \frac{c_s \rho}{g} u_*^b \left[\frac{1}{u_*} - \frac{2u_{*t}}{u_*^2} - \frac{3u_{*t}^2}{u_*^3} \right] \quad (4.18)$$

4.3 Constraints from Multi-Satellite Observations

4.4 Experiment Design

4.5 Constrained Dust Emission Scheme

4.6 Validations

4.7 Summary

CHAPTER 5

SUMMARY AND OUTLOOK

5.1 Summary of the Dissertation

5.2 Main Conclusions of This Work

5.3 Outlook and Future Work

APPENDIX A

ABBREVIATIONS AND ACRONYMS

APPENDIX B

SYMBOLS

REFERENCES

- Boucher, O., et al. (2013), *Clouds and Aerosols. In Climate Change 2013: The Physical Science Basis. Contribution of Working Group I to the Fifth Assessment Report of the Intergovernmental Panel on Climate Change [Stocker T.F., et al. (eds.)]*, p. 571–658, Cambridge University Press, Cambridge, United Kingdom and New York, NY, USA. [4.1](#)
- Burrows, S. M., T. Butler, P. Jockel, H. Tost, A. Kerkweg, U. Poschl, and M. G. Lawrence (2009), Bacteria in the global atmosphere. part 2: Modeling of emissions and transport between different ecosystems, *Atmospheric Chemistry and Physics*, 9(23), 9281–9297. [1.1](#)
- Byrd, R. H., P. Lu, J. Nocedal, and C. Zhu (1995), A limited memory algorithm for bound constrained optimization, *SIAM Journal on Scientific Computing*, 16, 1190–1208. [2.1](#)
- Carslaw, K. S., O. Boucher, D. V. Spracklen, G. W. Mann, J. G. L. Rae, S. Woodward, and M. Kulmala (2010), A review of natural aerosol interactions and feedbacks within the earth system, *Atmos. Chem. Phys.*, 10(4), 1701–1737, aCP. [4.1](#)
- Ginoux, P., M. Chin, I. Tegen, J. M. Prospero, B. Holben, O. Dubovik, and S.-J. Lin (2001), Sources and distributions of dust aerosols simulated with the gocart model, *J. Geophys. Res.*, 106(D17), 20,255–20,273. [4.1](#)
- Ginoux, P., J. M. Prospero, T. E. Gill, N. C. Hsu, and M. Zhao (2012), Global-scale attribution of anthropogenic and natural dust sources and their emission rates based on modis deep blue aerosol products, *Reviews of Geophysics*, 50(3), RG3005. [4.1](#)
- Griffin, D., V. Garrison, J. Herman, and E. Shinn (2001), African desert dust in the caribbean atmosphere: Microbiology and public health, *Aerobiologia*, 17(3), 203–213. [1.1](#)
- Hansen, P. C. (1998), *Rank-Deficient and Discrete Ill-Posed Problems: Numerical Aspects of Linear Inversion*, Soc. for Ind. and Appl. Math., Philadelphia, Pa. [2.1](#)

- Henze, D. K., A. Hakami, and J. H. Seinfeld (2007), Development of the adjoint of geos-chem, *Atmos. Chem. Phys.*, 7(9), 2413–2433. [1.1](#), [2.3](#)
- Henze, D. K., J. H. Seinfeld, and D. T. Shindell (2009), Inverse modeling and mapping us air quality influences of inorganic pm2.5 precursor emissions using the adjoint of geos-chem, *Atmos. Chem. Phys.*, 9(16), 5877–5903. [2.3](#)
- Holben, B. N., et al. (1998), Aeronet - a federated instrument network and data archive for aerosol characterization, *Remote Sensing of Environment*, 66(1), 1–16. [4.1](#)
- Hsu, N. C., T. Si-Chee, M. D. King, and J. R. Herman (2006), Deep blue retrievals of asian aerosol properties during ace-asia, *Geoscience and Remote Sensing, IEEE Transactions on*, 44(11), 3180–3195. [4.1](#)
- Hsu, N. C., M. J. Jeong, C. Bettenhausen, A. M. Sayer, R. Hansell, C. S. Seftor, J. Huang, and S. C. Tsay (2013), Enhanced deep blue aerosol retrieval algorithm: The second generation, *Journal of Geophysical Research: Atmospheres*, 118(16), 9296–9315. [4.1](#)
- Huneeus, N., et al. (2011), Global dust model intercomparison in aerocom phase i, *Atmos. Chem. Phys.*, 11(15), 7781–7816. [4.1](#)
- Husar, R. B., et al. (2001), Asian dust events of april 1998, *J. Geophys. Res.*, 106(D16), 18,317–18,330. [4.1](#)
- Jiang, Z., D. B. A. Jones, M. Kopacz, J. Liu, D. K. Henze, and C. Heald (2011), Quantifying the impact of model errors on top-down estimates of carbon monoxide emissions using satellite observations, *Journal of Geophysical Research: Atmospheres*, 116(D15), D15,306. [2.3](#)
- Jickells, T. D., et al. (2005), Global iron connections between desert dust, ocean biogeochemistry, and climate, *Science*, 308(5718), 67–71. [1.1](#)
- Kaufman, Y. J., D. Tanre, and O. Boucher (2002), A satellite view of aerosols in the climate system, *Nature*, 419, 215 – 223. [4.1](#)
- King, M. D., Y. J. Kaufman, D. Tanre, and T. Nakajima (1999), Remote sensing of tropospheric aerosols from space: Past, present, and future, *Bulletin of the American Meteorological Society*, 80(11), 2229–2259. [4.1](#)

- Kopacz, M., D. J. Jacob, D. K. Henze, C. L. Heald, D. G. Streets, and Q. Zhang (2009), Comparison of adjoint and analytical bayesian inversion methods for constraining asian sources of carbon monoxide using satellite (mopitt) measurements of co columns, *J. Geophys. Res.*, *114*(D4), D04,305. [2.3](#)
- Kopacz, M., et al. (2010), Global estimates of co sources with high resolution by adjoint inversion of multiple satellite datasets (mopitt, airs, sciamachy, tes), *Atmos. Chem. Phys.*, *10*(3), 855–876. [2.3](#)
- Kopacz, M., D. L. Mauzerall, J. Wang, E. M. Leibensperger, D. K. Henze, and K. Singh (2011), Origin and radiative forcing of black carbon transported to the himalayas and tibetan plateau, *Atmos. Chem. Phys.*, *11*(6), 2837–2852. [2.3](#)
- Martonchik, J. V., R. A. Kahn, and D. J. Diner (2009), *Retrieval of aerosol properties over land using MISR observations*, Springer, Berlin. [4.1](#)
- Parrington, M., et al. (2012), The influence of boreal biomass burning emissions on the distribution of tropospheric ozone over north america and the north atlantic during 2010, *Atmospheric Chemistry and Physics*, *12*(4), 2077–2098. [2.3](#)
- Ravi, S., et al. (2011), Aeolian processes and the biosphere, *Reviews of Geophysics*, *49*(3), RG3001. [4.1](#)
- Rodgers, C. D. (2000), *Inverse Methods for Atmospheric Sounding: Theory and Practice*, World Scientific, Singapore. [2.1](#)
- Satheesh, S. K., and K. Krishna Moorthy (2005), Radiative effects of natural aerosols: A review, *Atmospheric Environment*, *39*(11), 2089–2110. [4.1](#)
- Shao, Y., et al. (2011), Dust cycle: An emerging core theme in earth system science, *Aeolian Research*, *2*(4), 181–204. [4.1](#)
- Streets, D. G., et al. (2003), An inventory of gaseous and primary aerosol emissions in asia in the year 2000, *J. Geophys. Res.*, *108*(D21), 8809. [1.1.1](#)
- Tegen, I., and I. Fung (1994), Modeling of mineral dust in the atmosphere: Sources, transport, and optical thickness, *J. Geophys. Res.*, *99*(D11), 22,897–22,914. [4.1](#)
- Tegen, I., A. A. Lacis, and I. Fung (1996), The influence on climate forcing of mineral aerosols from disturbed soils, *Nature*, *380*(6573), 419–422. [4.1](#)

- Tegen, I., M. Werner, S. P. Harrison, and K. E. Kohfeld (2004), Relative importance of climate and land use in determining present and future global soil dust emission, *Geophys. Res. Lett.*, *31*(5), L05,105. [4.1](#)
- Textor, C., et al. (2006), Analysis and quantification of the diversities of aerosol life cycles within aerocom, *Atmos. Chem. Phys.*, *6*(7), 1777–1813. [4.1](#)
- Toon, O. B. (2003), Atmospheric science: African dust in florida clouds, *Nature*, *424*(6949), 623–624, 10.1038/424623a. [4.1](#)
- Uno, I., et al. (2006), Dust model intercomparison (dmip) study over asia: Overview, *J. Geophys. Res.*, *111*(D12), D12,213. [4.1](#)
- Wecht, K. J., D. J. Jacob, S. C. Wofsy, E. A. Kort, J. R. Worden, S. S. Kulawik, D. K. Henze, M. Kopacz, and V. H. Payne (2012), Validation of tes methane with hippo aircraft observations: implications for inverse modeling of methane sources, *Atmospheric Chemistry and Physics*, *12*(4), 1823–1832. [2.3](#)
- Zender, C. S., H. Bian, and D. Newman (2003), Mineral dust entrainment and deposition (dead) model: Description and 1990s dust climatology, *J. Geophys. Res.*, *108*(D14), 4416. [4.1](#)
- Zhu, C., R. H. Byrd, P. Lu, and J. Nocedal (1994), L-bfgs-b: a limited memory fortran code for solving bound constrained optimization problems, *Technique report*, Northwestern University. [2.1](#)
- Zoogman, P., et al. (2011), Ozone air quality measurement requirements for a geostationary satellite mission, *Atmospheric Environment*, *45*(39), 7143 – 7150. [2.3](#)

LIST OF PUBLICATIONS

List my publication here